Bio-Design and Manufacturing (2022) 5:529–539
https://doi.org/10.1007/s42242-022-00186-3

RESEARCH ARTICLE

# Modulating vectored non-covalent interactions for layered assembly with engineerable properties

Jiahao Zhang[1,2] · Sarah Guerin[3] · Haoran Wu[1,2] · Bin Xue[4] · Yi Cao[4] · Syed A. M. Tofail[3] · Yancheng Wang[1,5] · Damien Thompson[3] · Wei Wang[4] · Kai Tao[1,2,5] · Deqing Mei[1,5] · Ehud Gazit[6,7]

Received: 1 August 2021 / Accepted: 14 January 2022 / Published online: 14 February 2022


## Abstract

Vectored non-covalent interactions—mainly hydrogen bonding and aromatic interactions—extensively contribute to (bio)-organic self-assembling processes and significantly impact the physicochemical properties of the associated superstructures. However, vectored non-covalent interaction-driven assembly occurs mainly along one-dimensional (1D) or three-dimensional (3D) directions, and a two-dimensional (2D) orientation, especially that of multilayered, graphene-like assembly, has been reported less. In this present research, by introducing amino, hydroxyl, and phenyl moieties to the triazine skeleton, supramolecular layered assembly is achieved by vectored non-covalent interactions. The planar hydrogen bonding network results in high stability, with a thermal sustainability of up to about 330 °C and a Young's modulus of up to about 40 GPa. Upon introducing wrinkles by biased hydrogen bonding or aromatic interactions to disturb the planar organization, the stability attenuates. However, the intertwined aromatic interactions prompt a red edge excitation shift effect inside the assemblies, inducing broad-spectrum fluorescence covering nearly the entire visible light region (400–650 nm). We show that bionic, superhydrophobic, pillar-like arrays with contact angles of up to about 170° can be engineered by aromatic interactions using a physical vapor deposition approach, which cannot be realized through hydrogen bonding. Our findings show the feasibility of 2D assembly with engineerable properties by modulating vectored non-covalent interactions.

Jiahao Zhang and Sarah Guerin have contributed equally to this work.

✉ Bin Xue
xuebinnju@nju.edu.cn

✉ Damien Thompson
Damien.Thompson@ul.ie

✉ Kai Tao
kai.tao@zju.edu.cn

[1] State Key Laboratory of Fluid Power and Mechatronic Systems, School of Mechanical Engineering, Zhejiang University, Hangzhou 310027, China

[2] Future Science Research Institute, Hangzhou Global Scientific and Technological Innovation Center, Zhejiang University, Hangzhou 311200, China

[3] Department of Physics and Bernal Institute, University of Limerick, Castletroy, Co. Limerick, Limerick V94T9PX, Ireland

[4] National Laboratory of Solid State Microstructure, Department of Physics, Nanjing University, Nanjing 210093, China

[5] Key Laboratory of Advanced Manufacturing Technology of Zhejiang Province, School of Mechanical Engineering, Zhejiang University, Hangzhou 310027, China

[6] School of Molecular Cell Biology and Biotechnology, George S. Wise Faculty of Life Sciences, Tel Aviv University, 6997801 Tel Aviv, Israel

[7] Department of Materials Science and Engineering, Iby and Aladar Fleischman Faculty of Engineering, Tel Aviv University, 6997801 Tel Aviv, Israel

**Graphic abstract**

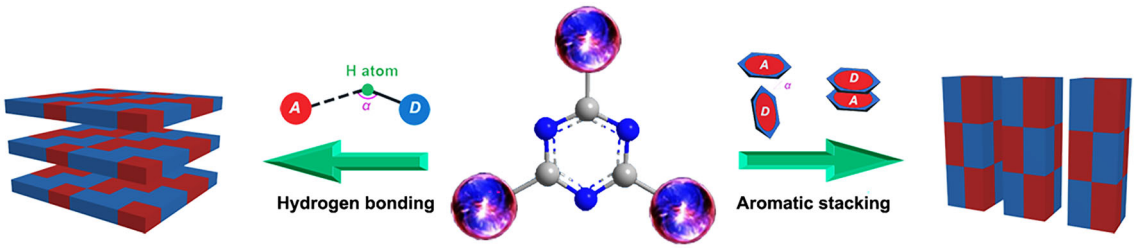


**Keywords** Vectored non-covalent interactions · Layered assembly · Supramolecular graphene · Engineerable properties · Physical vapor deposition

## Introduction

Self-assembly, driven by non-covalent interactions, is ubiquitous in (bio)-organic supramolecular systems [1–4]. In contrast to directionless non-covalent interactions of arbitrary orientations (such as non-specific van der Waals interactions and hydrophobic interactions), vectored non-covalent interactions with explicit directions, including hydrogen bonding and aromatic interactions (Scheme 1), can dictate self-assembly directions, thereby determining the properties of the supramolecular structures [5–8].

Peptide-based self-assembly is a prominent example of self-association mediated by hydrogen bonding [9–11]. During the self-assembly process, hydrogen bonding interactions drive the peptide molecules to cluster into diverse secondary structures (β-sheets, α-helices, etc.) and then coalesce into superstructures [12–14]. A well-known self-assembly case driven by aromatic interactions is that of aggregation-induced emission systems (such as tetraphenyl ethylene self-assemblies) [15, 16], in which the conformational restriction created by the aromatic network endows the assemblies with remarkable photoluminescence [17]. Recently, researchers have increasingly demonstrated that the coupling of two vectored non-covalent interactions, for example in aromatic short peptides [3, 6, 18–20] and organic small molecule semiconductors [21, 22], can result in intricate assemblies with enhanced optical, electronic, or mechanical properties [5, 23]. However, it should be noted that most vectored non-covalent interaction-assembled networks are in the 1D or 3D directions, while 2D (layered)-oriented organization has been reported less [24–26]. Correspondingly, the effect of vectored non-covalent interactions on 2D organization properties, along with the engineering of layered assemblies, is yet to be examined.

We designed heterocyclic triazine-based building blocks, including melamine (**M**), cyanuric acid (**C**), and triphenyl-triazine (**TPTA**), which have triazine backbones modified with amino, hydroxyl, and phenyl moieties, respectively (Figs. 1a-i, 1b-i, and 1d-i), to utilize vectored non-covalent interactions for 2D assembly, and in particular, to study the effects of vectored non-covalent interactions on the properties of the layered superstructures.

## Materials and methods

### Materials

Melamine (**M**), cyanuric acid (**C**), and triphenyl-triazine (**TPTA**) were purchased from Sigma Aldrich (Rehovot, Israel). All the materials were used as received without further purification. Water was processed using a Millipore® purification system (Darmstadt, Germany) with a minimum resistivity of 18.2 MΩ·cm.

### Crystal preparation

The sample powders were dissolved in water to a concentration of 10.0 mM. The solutions were then incubated

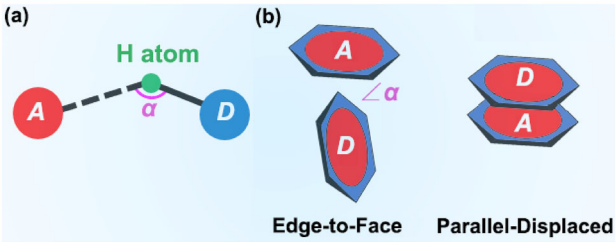


**Scheme 1** Schematic representation of vectored non-covalent interactions mediating self-assembling systems. **a** Hydrogen bonding. **b** Two types of commonly found aromatic interactions: edge-to-face (T-shaped) and parallel-displaced (face-to-face). *A* and *D* designate acceptor and donor atoms, respectively, which synergistically induce dipole moments and the directions of the interactions. *α* represents the non-covalent bond angle. For hydrogen bonding, the bond strength attenuates with *α* deviating from 180°. For π-π interactions, *α* can take several optimal values—for example, in the edge-to-face and parallel-displaced motifs shown

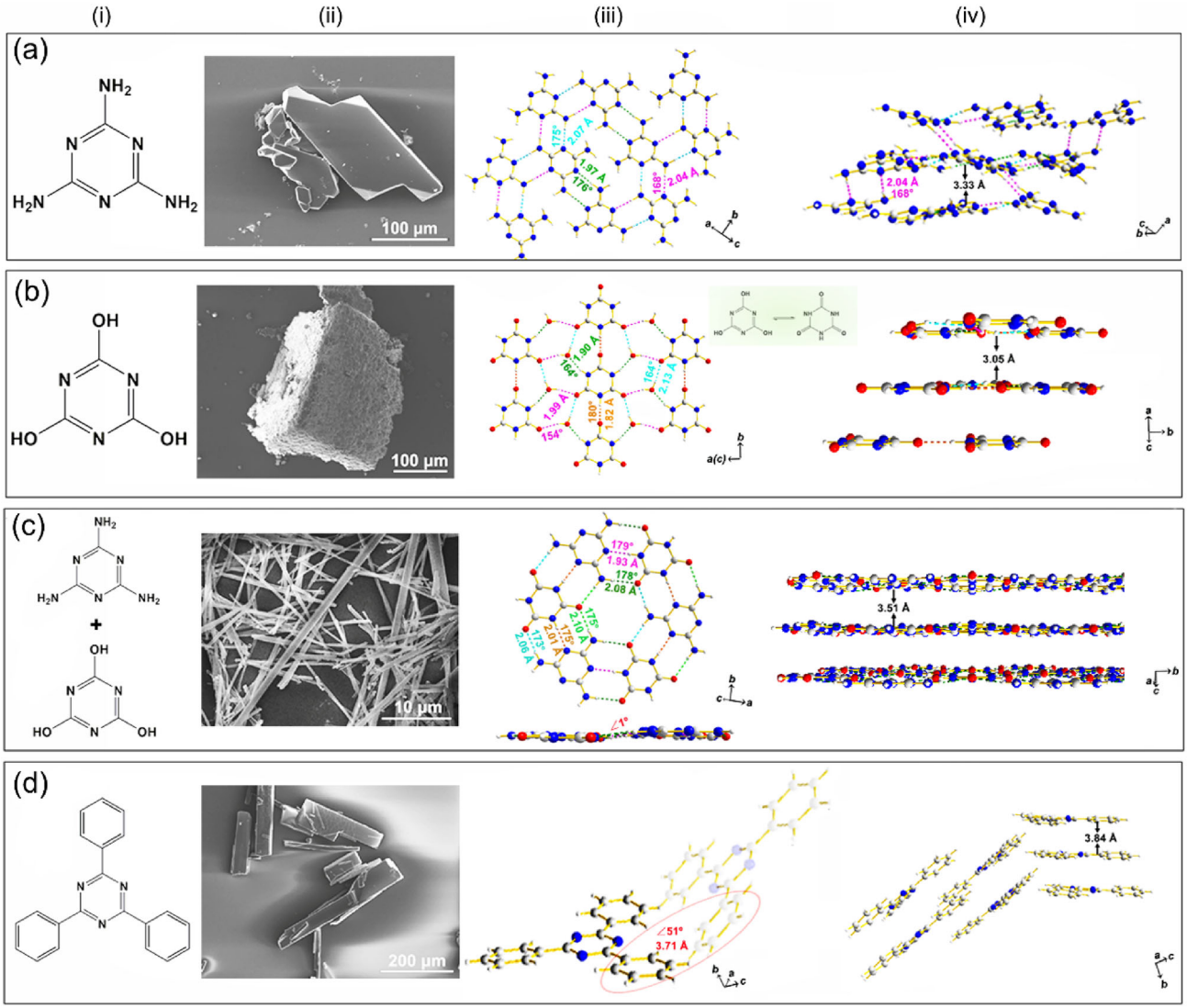


**Fig. 1** Crystallographic characterization of the vectored non-covalent interaction-driven assemblies. **a M**, **b C**, **c M + C**, **d TPTA**. (i) Molecular structures. (ii) SEM images, (iii) and (iv) crystallographic structures viewed in the plane or from the side. The carbon, oxygen, nitrogen, and hydrogen atoms are shown as gray, red, blue, and white balls. Covalent bonds are shown as yellow sticks. The dotted lines in (iii) and (iv) represent the hydrogen bonds. The colors distinguish different groups, with the bond length and bond angle values labeled in the corresponding locations. Interlayer separations driven by aromatic interactions in the direction normal to the layers (and for **M**, also hydrogen bonding) are marked in black in (iv) and (iii) in (d)

in a 90 °C water bath for 10 min, followed by filtration using 0.45 μm polyvinylidene fluoride (PVDF) membranes (Merck Millipore, Carrigtwohill, Ireland). Subsequently, crystals appeared and reached their maximum sizes within 30 days. The solutions were centrifuged, and the crystals were collected for later use.

## Scanning electron microscopy (SEM)

The solution containing the crystals was placed onto a clean glass slide, allowed to adsorb for a few seconds, and excess liquid was removed using a filter paper. The slide was then coated with Cr and observed under a JSM-6700 field emission scanning electron microscope (JEOL, Tokyo, Japan) operated at 10 kV.

## Thermal gravimetric analysis (TGA)

TGA experiments were performed using a TA Instruments (USA) module, SDT 2950, in a temperature range between 25 and 500 °C at a heating rate of 10 °C/min under a dry, ultrahigh-purity, argon atmosphere.

## Theoretical calculations

Electromechanical properties were predicted from periodic density functional theory (DFT) [27] calculations using the *Vienna Ab-initio Simulation Package* (*VASP*) [28] code. Electronic structures were calculated using the Perdew–Burke–Ernzerhof (PBE) functional [29] with Grimme-D3 dispersion corrections [30] and projector augmented wave (PAW) pseudopotentials [31]. The crystal structure was relaxed using a plane wave cutoff of 600 eV with a $4 \times 4 \times 4$ $k$-point grid. A finite difference method was used to calculate the stiffness tensor of the optimized crystal, with each atom being displaced in each direction by $\pm 0.01$ Å (1 Å $= 10^{-10}$ m). Piezoelectric strain constants and dielectric tensors were calculated by density functional perturbation theory (DFPT) [32], using a plane wave cutoff of 1000 eV and a $k$-point sampling of $2 \times 2 \times 2$. Young's moduli were derived from the stiffness and its inverse compliance matrix components using the Voigt–Reuss–Hill method [33, 34]. Crystal structures were visualized using VESTA [35].

## Young's modulus measurement

Atomic force microscopy (AFM) experiments were carried out using a commercial atomic force microscope (JPK, Nanowizard IV, Berlin, Germany). The Young's modulus and point stiffness were detected using the QI mode (conditions—pixels: $126 \times 126$; $Z$ length: 0.3 μm; extend and retract speed: 30 μm/s; $Z$ resolution: 80,000 Hz). The force curves were obtained using commercial software from JPK and analyzed with *JPK Data Processing* (version 7.0.97). All the experiments were performed with RTESPA-525 cantilevers (Bruker, USA, tip radius: about 8 nm, spring constant: 200 N/m) in air at room temperature and the maximum loading force was set as 800 nN. In a typical experiment, the crystals were cast on the surface of a glass substrate, and the cantilever extended to the crystal at a constant speed of 30 μm/s. The cantilever was held on the crystal surface at a constant force of 800 pN. Then, the cantilever retracted and moved to another spot for the next cycle. The force–displacement curves were recorded, and the Young's modulus of the crystals could be calculated by fitting the extending curve with the Hertz model:

$$F = \frac{4}{3}\frac{E}{\left(1-\upsilon^2\right)}\sqrt{R}\delta^{3/2}, \quad (1)$$

in which $F$ corresponds to the force, $\delta$ corresponds to the depth of the crystal pressed by the cantilever tip, $R$ corresponds to the radius of the tip, $E$ is the Young's modulus of the crystals, and $\upsilon$ is the Poisson ratio ($\upsilon = 0.3$) [36, 37].

Each approaching force–deformation curve was fitted in a range of 15 nm from the contact point, or from the maximum indentation depth to the contact point if the former was less than 15 nm. The point stiffness of the crystals was determined as the normal force divided by the deformation of the sample and calculated from the force- displacement curves after deducting the deformation of the cantilever. Typically, 5–8 such regions were randomly selected on each crystal to construct an elasticity histogram. Three cantilevers of the same type were used in the experiments to exclude tip-to-tip dependency.

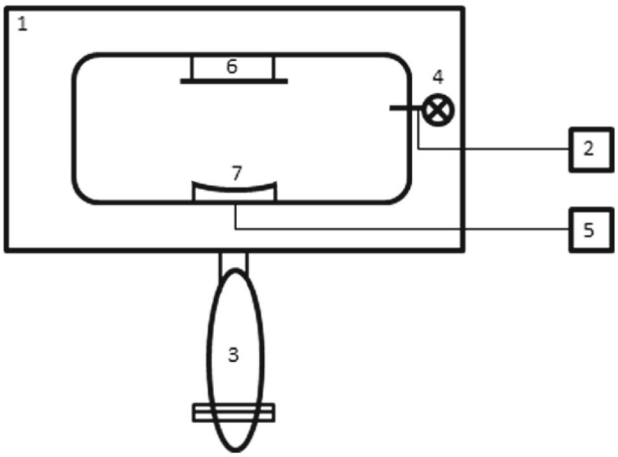


**Scheme 2** Schematic representation of the physical vapor deposition (PVD) system used for vectored non-covalent interaction assembly: (1) vacuum chamber, (2) vacuum control system, (3) vacuum turbo-molecular pump system, (4) vacuum gauge, (5) heating control system for sample powder holder, (6) substrate holder, (7) raw sample powder holder. To ensure the formation of the micro-structured arraying conformations, the distance between (6) and (7) was critical and was set at 1.5 cm

## Fluorescent microscopy characterization

The crystal samples were cast onto clean glass slides, and fluorescent microscopy measurements were taken using a Nikon Eclipse Ti Inverted Microscope (Nikon Instruments, Tokyo, Japan) under different filters and at ambient temperature.

## Physical vapor deposition (PVD)

In Scheme 2, we present the PVD system setup which was designed to assemble the vectored non-covalent interactions by thermal evaporation. The deposition procedure was conducted in a vacuum chamber (1), which contained the following elements: a vacuum control system (2), a turbo-molecular pump (3), a vacuum gauge (4), and a heating control system for the sample powder holder (5). The vacuum turbo-molecular pump system is able to decrease the vacuum pressure of the chamber to less than $5.0 \times 10^{-6}$ mbar. The substrate holder (6) was located above the precursor sample powder holder (7). The distance between (6) and (7) was

**Table 1** Deposition temperature routine used for physical vapor deposition (PVD)

| Temperature region (°C) | Duration time (min) |
|---|---|
| RT–60 | 10 |
| 60–160 | 10 |
| 160–220 | 20 |
| 220 | 15 |

critical to the formation of the array structures and was set to 1.5 cm in our experiment. The deposition temperature routine is shown in Table 1.

## Results and discussion

Scanning electron microscopy (SEM) experiments revealed that **M** and **C** self-assembled into platelike crystals (Figs. 1a-ii and 1b-ii). Crystallographic characterization demonstrated that the crystals were parallel-stacked, layer-by-layer crystals (Figs. 1a-iii, 1b-iii, and 1b-iv). Specifically, in the **M** case, the building blocks were planarly connected and formed layered structures through donor-H···acceptor, $N_{amino}$-H···$N_{triazine}$ hydrogen bonds with three distinct contact types identified with distances and angles of: 1.97 Å and 176°, 2.07 Å and 175°, 2.04 Å and 168° (Fig. 1a-iii). These are similar but not precisely the same, reflecting the slight tilting of the molecules to optimize simultaneously in-plane and interplane hydrogen bonding. In the interlayer direction, the layers were connected by the hydrogen bonding of 2.04 Å and 168°, the weakest H bond with the smallest bond angle among the three H bonds, which, together with interlayer aromatic stacking, creates an interval distance of 3.33 Å between adjacent layers (Fig. 1a-iv). Since only two amino groups in each **M** molecule contributed to the formation of the hydrogen bonding, with the other one left free (Fig. 1a-iii), the uneven hydrogen bonding distributions resulted in non-parallel layers and the formation of wrinkles (Fig.1a-iv). In the case of **C**, the water molecules extensively contributed to organization (Fig. 1b-iii). Previous studies have revealed that the participation of solvent molecules can significantly affect the structures and the properties of the assemblies [36, 38, 39]. Upon crystallization and the solvent molecules driving, the **C** molecule transformed to its tautomer by exchanging the locations of the hydrogen atoms (Fig. 1b-iii, inset), thus creating an extensive hydrogen bonding network. Specifically, except for two instances of hydrogen bonding of 1.82 Å and 180° ($N_{\mathbf{C}}$···H–$O_{\mathbf{C}}$) formed directly by two **C** molecules (Fig. 1b-iii), other sites on **C** formed three pairs of hydrogen bonding with water molecules: 1.90 Å and 164° ($N_{\mathbf{C}}$–H···$O_{water}$), 1.99 Å and 154° ($O_{water}$–H···$O_{\mathbf{C}}$), and 2.13 Å and 164° ($O_{water}$–H···$O_{\mathbf{C}}$). In contrast to the case of **M**, because all the oxygen and nitrogen atoms in each **C** molecule participated in the formation of hydrogen bonding, the distribution uniformity of the hydrogen bonding resulted in layer-by-layer planar organization with an interlayer distance of only 3.05 Å, smaller than that of the case of **M** (Fig. 1b-iv). Notably, the interlayer distance here for **C**, unlike for **M**, was motivated purely by aromatic interactions between the wrinkle-free layers.

It is well established that **M** and **C** can co-assemble by complementary base-pairing-like hydrogen bonding [40]. However, these complementary, vectored non-covalent bonds can be separated into two groups—one group composed of straight hydrogen bonding with a bond angle of nearly 180° along the *b* direction (a pair of $N_{\mathbf{M}}$–H···$O_{\mathbf{C}}$ interactions of 2.08 Å and 178° and a $N_{\mathbf{C}}$–H···$N_{\mathbf{M}}$ of 1.93 Å and 179°) and the other one comprising relatively curved bonds with bond angles of about 175° (three types of hydrogen bonding of $N_{\mathbf{M}}$–H···$O_{\mathbf{C}}$ of 2.10 Å and 175°, $N_{\mathbf{C}}$–H···$N_{\mathbf{M}}$ of 2.01 Å and 175°, $N_{\mathbf{M}}$–H···$O_{\mathbf{C}}$ of 2.06 Å and 173°) (Fig. 1c-iii, upper panel). Logically, the bond angle deviation between the two groups of hydrogen bonding induced a slight fluctuation of the uniformity, thus resulting in a small wrinkle of 1° of the organized layers (Fig. 1c-iii, lower panel). Notably, this structural perturbation could disturb the interlayer interactions, thus inducing layer-by-layer stacking with an interval distance of 3.51 Å (Fig. 1c-iv), which is larger than that of **C** alone.

It should be mentioned that the interlayer distances of the vectored non-covalent interaction-driven assemblies resemble those of graphite (about 3.4 Å) [41]. In particular, the exact distance could be finely tuned by reasonably controlling the organization of the vectored non-covalent interactions. Therefore, the crystallographic characterizations not

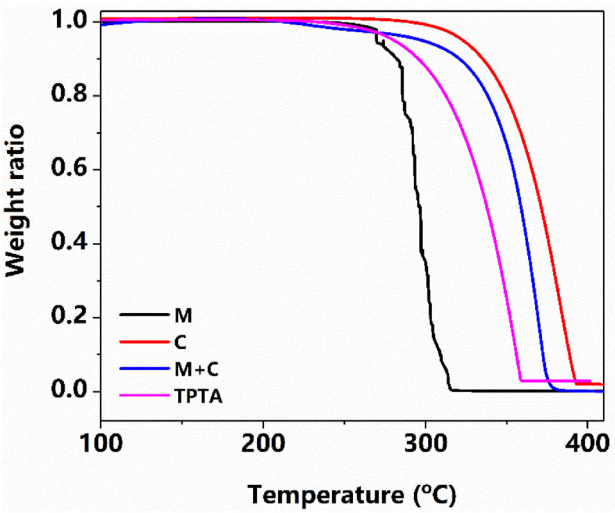


**Fig. 2** Thermal gravimetric analysis (TGA) curves of the vectored non-covalent interaction-driven assemblies

only confirmed the influence of the solvent molecules on self-assemblies but exemplified the feasibility of designing supramolecular "graphene-like" constructions with engineerable properties.

In contrast to the above systems, no hydrogen bonding was identified in the case of **TPTA**. Instead, edge-to-face (or T-type) π–π stacking dominated in the organization (Scheme 1b), with a dihedral angle of 51° between the interacting phenyl rings and a nearest interatomic distance of 3.71 Å (Fig. 1d-iii). In the interlayer direction, the adjacent phenyl rings formed parallel-displaced interactions with a separation of 3.84 Å (Fig. 1d-iv). This value is significantly larger than those in the other, straight-layered systems, with the tilted T-type aromatic interactions stretching to fill the distances between the layers and creating an intertwining, severely wrinkled assembly.

The different driving force networks and organization conformations imply distinct stabilities of the layered assemblies [37, 42]. At the macroscopic level, thermal gravimetric analysis (TGA) characterizations demonstrate that the **C** crystals showed the highest thermo-sustainability with a degradation point at 328 °C, followed by **M + C** (323 °C), **TPTA** (297 °C), and **M** (279 °C) (Fig. 2). We postulated that, together with the crystallographic characterizations, the homogeneous organization of lateral interactions coupled with short interlayer separation generate more robust assemblies [43]. According to this hypothesis, the evenly planar conformation conferred **C** and **M + C** superstructures a high thermal stability of > 300 °C. Once the uniformity was disturbed, such as by biasing hydrogen bonding in the case of **M** or inducing herring bone-like aromatic stacking in the **TPTA** case, the wrinkles in the layers reduced the order of the structures, resulting in compromised thermal stability with a degradation < 300 °C. Compared to the extensive intertwining of aromatic interactions inside the **TPTA** system, **M** showed a mixture of intralayer and interlayer hydrogen bonding (Figs. 1a and 1d), which produced rough layers and the lowest thermo-sustainability.

The diverse thermo-sustainability also suggests divergent mechanical properties in the self-assemblies [37, 42, 44]. Therefore, the elastic moduli of the crystals were predicted by DFT calculations (Figs. S1 and S2 in Supplementary Information). For single crystals, mechanical strength increases with improved alignment of the molecules [45]. Table 2 shows that the most thermostable **C** assembly displayed the highest axial strength ($c_{22}$ = 135 GPa) and a large Young's modulus value (28 GPa), consistent with the crystallographic analysis and TGA experiments. Compared to the **C** crystals, the **M** and **TPTA** assemblies showed a remarkably lower elastic anisotropy, along with smaller Young's modulus values of 26 and 14 GPa, respectively (Table 2). Specifically, in the **M** case, the wrinkled layers contributed to a $c_{max}$ of $c_{22}$ = 60 GPa, and a "zigzag" orientation of the molecules across the *ab* plane contributed to the highest shear stiffness among the four assemblies ($c_{min}$ = 9 GPa) (Fig. S1b in Supplementary Information). In the **TPTA** assembly, the highest axial strength was across the *ac* plane, with predicted values of $c_{11}$ = 24 GPa and $c_{33}$ = 25 GPa (Fig. S2a in Supplementary Information).

By contrast, the **M + C** co-crystals demonstrated the highest predicted Young's modulus of 37 GPa (Table 2). Similarly to the **C** crystals, the mechanical strength of the co-crystals reflects the closely stacked even planes (Figs. 1b-iv, 1c-iv and Fig. S2d online in Supplementary Information) [46]. However, the 32% enhancement in mechanical stability relative to that of the **C** crystals can be attributed to the lack of solvent molecules within the co-crystals, thus avoiding the weaker hydrogen bonding with smaller bond angles that occurred in the **C** assemblies (bond angles ranging from 154° to 164°). The highest axial strength was due to the very dense supramolecular packing along the *b* axis (Fig. 1c-iv and Fig. S2e in Supplementary Information), resulting in a predicted $c_{22}$ value of 86 GPa.

Thus, when the 2D layers are near-parallel to a crystallographic axis, as is the case for the **C** and **M + C** assemblies, a low stiffness is observed perpendicular to the layers [46, 47]. Applying a force along the *a* axis may easily push these layers together, as is reflected in a $c_{11}$ value of 14 GPa for the **C** crystals. Particularly, the resulting predicted $c_{33}$ value of 6 GPa for **M + C** co-crystals is, to the best of our knowledge, the smallest predicted longitudinal stiffness for a (bio)-organic crystal reported to date.

To test the DFT predictions, we applied nano-indentation through AFM to measure the micromechanical properties of the crystals (Figs. S3 and S4 in Supplementary Information) [37]. Specifically, the Young's moduli of the **C** and **M + C** crystals were 34.3 ± 5.4 GPa and 33.9 ± 5.9 GPa, respectively, which led to a point stiffness of 343.7 ± 66.8 N/m and 428.5 ± 59.8 N/m (Fig. 3), thus verifying strong supramolecular packing in the assemblies [14] and confirming the DFT predictions (Table 2). The measured Young's moduli along the thickness direction of the **M** and **TPTA** staggered crystals were 24.9 ± 2.6 GPa and 12.1 ± 3.2 GPa, respectively (Fig. 3). The weaker elasticity indicated lower point stiffnesses for these assemblies—of 204.1 ± 24.1 N/m and 142.8 ± 21.2 N/m for **M** and **TPTA**, respectively. The agreement between the nano-indentation measurements and DFT calculations supports our hypothesis that we can "dial in" desired physical properties in 2D assemblies by logically modulating the vectored non-covalent driving forces.

In addition to directing the mechanical properties of the assemblies, layered stacking may also regulate the degree of freedom in the interlayer direction. Therefore, the optical properties of the assemblies were further investigated. Fluorescent microscopy characterizations demonstrated that all four crystals showed fluorescence in the blue–green light

**Table 2** Computed elastic constants of the **M**, **C**, **M + C**, and **TPTA** crystals

| Elastic stiffness constant | M | C | M + C | TPTA |
|---|---|---|---|---|
| $c_{11}$ | 42 | 14 | 51 | 24 |
| $c_{22}$ | 60 | 135 | 86 | 19 |
| $c_{33}$ | 30 | 76 | 6 | 25 |
| $c_{44}$ | 9 | 11 | 5 | -2 |
| $c_{55}$ | 18 | 11 | 16 | 7 |
| $c_{66}$ | 14 | 2 | 9 | 1 |
| Young's modulus | 26 | 28 | 37 | 14 |

All values are in GPa. $c_{11}$, $c_{22}$, and $c_{33}$ are the longitudinal stiffness constants, while the shear stiffness constants are $c_{44}$, $c_{55}$, and $c_{66}$

region (400–550 nm; Figs. 4a–4d) due to the aggregation-induced quantum confinement effect at the non-covalent interfaces [11, 19, 48]. However, in the longer wavelength region (>550 nm), such as in the cyanine 3 (CY3)-filter range (590–650 nm), only **TPTA** crystals showed strong fluorescence with a discernibly emissive contour of the crystals (Fig. 4e-iv)—a characteristic feature of the red edge excitation shift (REES) phenomenon [40]. In contrast, the other three crystals presented negligible photoluminescence in the long wavelength region, with only some bright dots in the images (Figs. 4e-i–4e-iii).

The REES phenomenon arises from the fact that the conformational relaxation time is less than that required for fluorescence lifetime, thus giving the assemblies diverse colors of emission under different excitations [49]. We suggest that in our system, during the relaxation of highly restricted surrounding molecules with respect to the excited triazine fluorophores, various intermediate states (*I* state) between the initial excited state (Franck–Condon state, *FC* state) and the final relaxed state (*R* state) were formed to minimize the interaction energy, thus resulting in the REES phenomenon (Scheme 3) [38]. In the case of **TPTA**, the extensively intertwined phenyl rings strongly restricted the

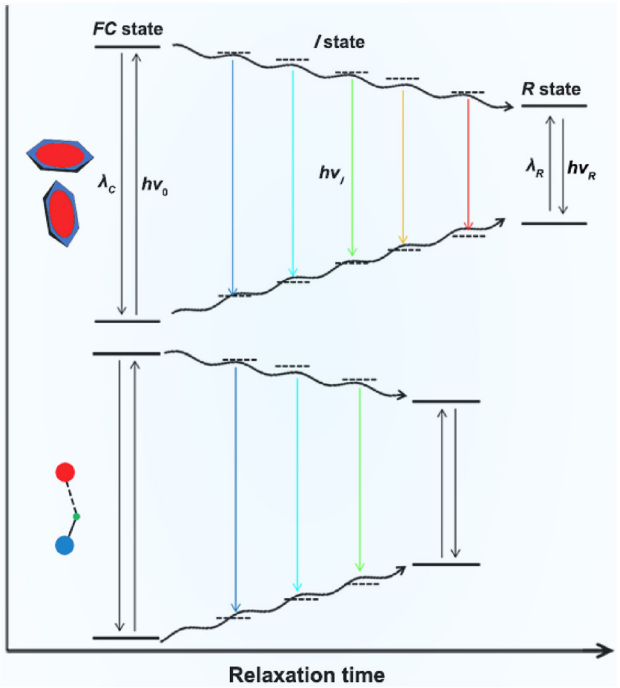


**Scheme 3** Schematic representation showing the REES phenomenon induced by the vectored non-covalent interactions. Upper panel: aromatic interactions; lower panel: hydrogen bonding. The "*I*" state refers to one of the intermediate states between the initial excited state (*FC* state) and the final relaxed state (*R* state). $\nu_0$, $\nu_i$, and $\nu_R$ represent the frequencies corresponding to the *FC*, *I*, and *R* states, respectively ($\nu_0 > \nu_i > \nu_R$), while $\lambda_C$ and $\lambda_R$ denote the maximal emission wavelengths associated with these states

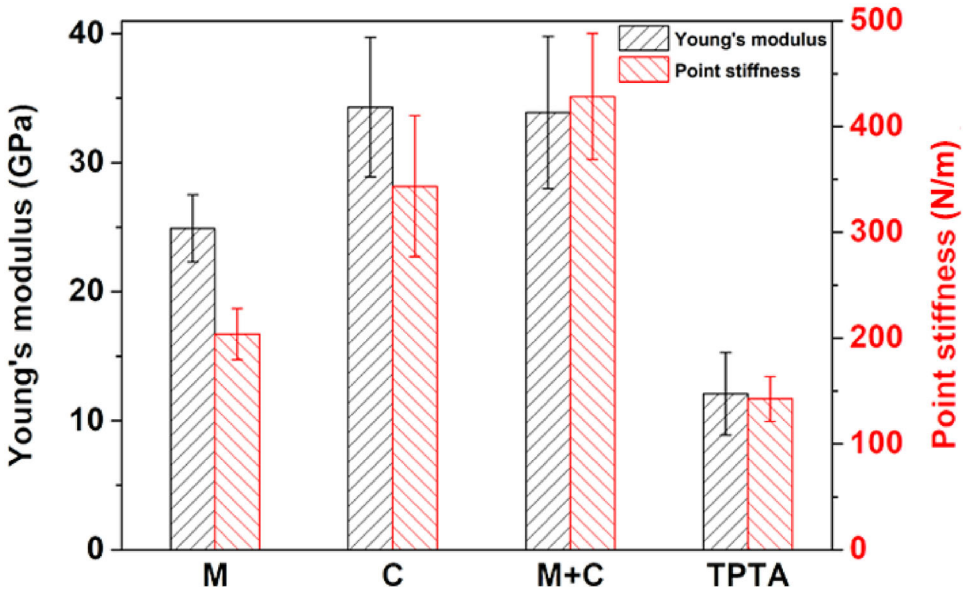


**Fig. 3** Measured mechanical properties of the vectored non-covalent interaction-driven self-assemblies

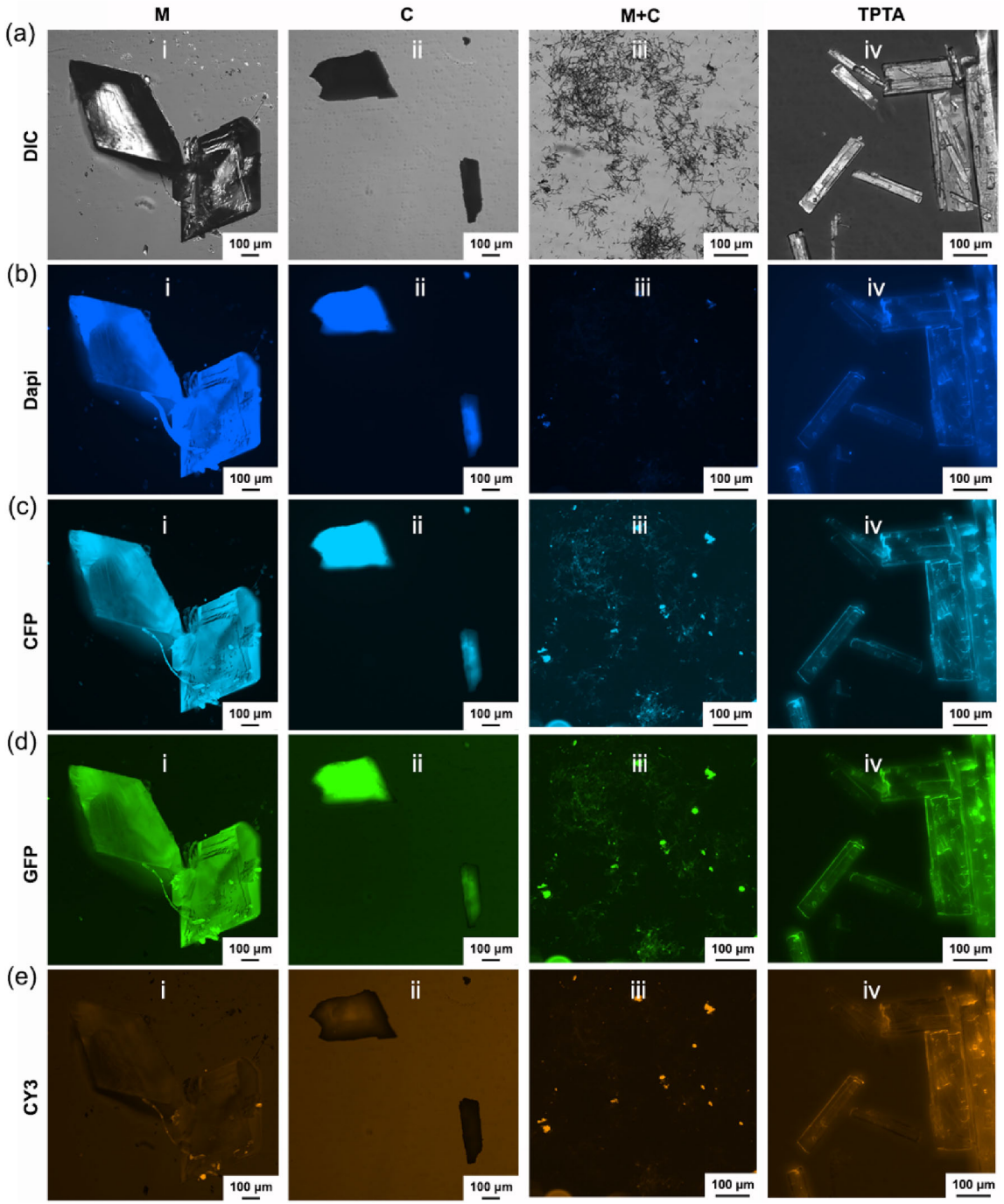


**Fig. 4** Fluorescent microscopy images of the vectored non-covalent interaction-driven self-assemblies. From left to right: **M**, **C**, **M + C**, **TPTA**. **a** DIC: differential interference contract mode; **b** Dapi: 4',6-diamidino-2-phenylindole filter (Excitation (Ex): 340–380 nm, Emission (Em): 435–485 nm); **c** CFP: cyan fluorescent protein filter (Ex: 420–445 nm, Em: 460–510 nm); **d** GFP: green fluorescent protein filer (Ex: 455–485 nm, Em: 500–545 nm); **e** CY3: (Ex: 528–553 nm, Em: 590–650 nm)

potential motions of the molecules, thus prolonging the relaxation time and giving the assemblies a broad-spectrum emission covering nearly the entire visible light region (Scheme 3, upper panel). However, in the other three systems, the planar organization allowed the molecules to move along the interplane direction with higher degrees of freedom. This could have shortened the relaxation time and attenuated the number of electron transitions and so lowered emission intensities, which finally resulted in an attenuated REES effect (Scheme 3, lower panel).

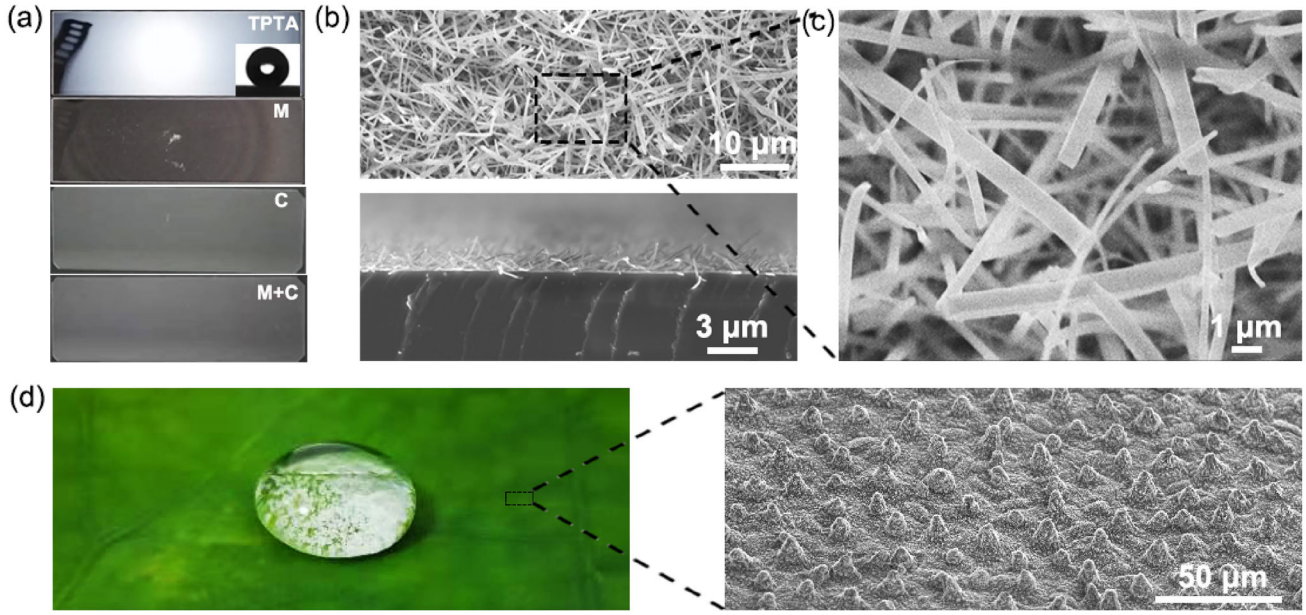


**Fig. 5** Micro-structured arrays of **TPTA** assemblies created via thermal evaporation. **a** Photograph of the arraying film after the PVD procedure. The inset shows the photographed superhydrophobic 166° contact angle of a water droplet on the film. **b** SEM images of the arrays. Top panel: vertical view, bottom panel: lateral view. **c** High-magnification SEM image of the area marked by the rectangle in Panel (**b**). **d** Left panel: photograph showing the superhydrophobic nature of the lotus leaf (photograph by J. H. Zhang). Right panel: SEM image of the pillar-like microstructures at the surface of the lotus leaf

Besides the REES effect, the increased mechanical softness of the intertwined conformation suggests that the aromatic interaction networks can be, to a large extent, engineered [50]. For this purpose, a physical vapor deposition (PVD) strategy was used to trigger the assembly of the vectored non-covalent interactions and to simultaneously align organization for large-scale fabrication [51]. Figure 5a shows that upon the thermal evaporation of **TPTA** (for experimental details, see Experimental Section), a white organic film was deposited on the glass substrate. By contrast, no apparent change was observed in the hydrogen bonding-mediated **M**, **C**, and **M + C** assembling systems. This demonstrates that compared to even layer-by-layer stacking driven by straight, in-plane hydrogen bonding, the intertwining of herring bone-like aromatic interactions is more readily organized under thermal evaporation conditions [52]. SEM characterization confirmed the longitudinally grown crystals inside the film (Figs. 5b and 5c). Lateral SEM imaging showed pillar-like array conformations (Fig. 5b, lower panel). According to the Young equation ($\omega\left(\gamma_{gs} - \gamma_{ls}\right) = \gamma_{gl}\cos\theta'$), the pillar-arraying structures significantly increased the roughness ($\omega$) of the substrate, producing a superhydrophobic film with a measured contact angle of $166.4° \pm 4.6°$ (inset of Fig. 5a), similar to the lotus, leaflike microstructures (Fig. 5d) [53]. The results demonstrate that bionic, micro-structured arrays can be engineered through the thermal evaporation-induced assembly of aromatic interactions. Particularly, it should be noted that the PVD approach can avoid the use of solvents, especially that of the organic solvents extensively used in conventional micro-electromechanical systems [54] and micro-structured film manufacturing fields [55], thus reducing contamination and cost.

## Conclusions

In conclusion, by introducing amino, hydroxyl, and phenyl moieties to the triazine skeleton, layered organization was realized by vectored non-covalent interactions including hydrogen bonding and aromatic interactions. The planar uniformity significantly promoted the mechanical stability and thermal sustainability of the assemblies, compared to assemblies with wrinkles due to biased hydrogen bonding or herringbone-like aromatic interactions. The intertwined nature of the aromatic, interaction-driven assemblies resulted in an REES effect conferring broad-spectrum emission covering nearly the entire visible light region. It also allowed easy alignment upon thermal evaporation. Thus, we were able to engineer purely organic, optically active, superhydrophobic arraying architectures. In the long term, diverse modification strategies, such as conjugating diverse functional groups to the triazine skeleton [56], flexible assembly approaches (co-assembly, crystallization in different solvents), and the modulation of the heating evaporation parameters (heating temperature, distance between sample powder holder and substrate, introduction of external electromagnetic fields,

etc.), can be utilized to further tune the organization of layering to fabricate devices with unique mechanical, optical, or electronic properties based on the vectored non-covalent interactions.

**Supplementary Information** The online version contains supplementary material available at https://doi.org/10.1007/s42242-022-00186-3.

**Acknowledgements** This work was supported by the Fund for Creative Research Groups of National Natural Science Foundation of China (No. 51821093), the National Natural Science Foundation of China (Nos. 52175551, 52075484) (KT and DM), the National Key Research and Development Program (SQ2021YFE010405) (KT) and Science Foundation Ireland (SFI) through awards Nos. 15/CDA/3491 and 12/RC/2275_P2 (DT), and computing resources at the SFI/Higher Education Authority Irish Center for High-End Computing (ICHEC) (SG and DT). The authors thank Dr. Sigal Rencus-Lazar for language editing and the members of all the laboratories for helpful discussions.

**Author contributions** All authors contributed to this manuscript and gave permission for the final version of the publication. BX, DT, and KT conceived and designed the work; JZ, HW, YW, and DM conducted the crystal growth and further characterizations; BX, YC, and WW conducted the Young's model measurement; JZ, HW, and EG performed the TGA experiments; JZ, HW, YW, DM, and EG fabricated the PVD system and the coating film; SG, SAMT, and DT carried out theoretical calculations; JZ and SG coordinated all the work, analyzed the results, wrote and edited the manuscript with input from all authors.

## Declarations

**Conflict of interest** The authors declare that there is no conflict of interest.

**Ethical approval** This study does not contain any studies with human or animal subjects performed by any of the authors.

## References

1. Aida T, Meijer EW, Stupp SI (2018) Functional supramolecular polymers. Science 335:813–817. https://doi.org/10.1126/science.1205962
2. Whitesides GM, Grzybowski B (2002) Self-assembly at all scales. Science 295:2418–2421. https://doi.org/10.1126/science.1070821
3. Yan X, Zhu P, Li J (2010) Self-assembly and application of diphenylalanine-based nanostructures. Chem Soc Rev 39:1877–1890. https://doi.org/10.1039/b915765b
4. Yuan C, Ji W, Xing R et al (2019) Hierarchically oriented organization in supramolecular peptide crystals. Nat Rev Chem 3:567–588. https://doi.org/10.1038/s41570-019-0129-8
5. Tao K, Makam P, Aizen R et al (2017) Self-assembling peptide semiconductors. Science. https://doi.org/10.1126/science.aam9756.
6. Fleming S, Ulijn RV (2014) Design of nanostructures based on aromatic peptide amphiphiles. Chem Soc Rev 43:8150–8177. https://doi.org/10.1039/c4cs00247d
7. Hong Y, Lam JWY, Tang BZ (2011) Aggregation-induced emission. Chem Soc Rev 40:5361–5388. https://doi.org/10.1039/C1CS15113D
8. Zhao X, Pan F, Xu H et al (2010) Molecular self-assembly and applications of designer peptide amphiphiles. Chem Soc Rev 39:3480–3498. https://doi.org/10.1039/b915923c
9. Ke PC, Sani MA, Ding F et al (2017) Implications of peptide assemblies in amyloid diseases. Chem Soc Rev 46:6492–6531. https://doi.org/10.1039/c7cs00372b
10. Zhang S (2003) Fabrication of novel biomaterials through molecular self-assembly. Nat Biotechnol 21:1171–1178. https://doi.org/10.1038/nbt874
11. Sun B, Tao K, Jia Y et al (2019) Photoactive properties of supramolecular assembled short peptides. Chem Soc Rev 48:4387–4400. https://doi.org/10.1039/c9cs00085b
12. Tao K, Levin A, Adler-Abramovich L et al (2016) Fmoc-modified amino acids and short peptides: simple bio-inspired building blocks for the fabrication of functional materials. Chem Soc Rev 45:3935–3953. https://doi.org/10.1039/c5cs00889a
13. Wei G, Xi W, Nussinov R et al (2016) Protein ensembles: how does nature harness thermodynamic fluctuations for life? The diverse functional roles of conformational ensembles in the cell. Chem Rev 116:6516–6551. https://doi.org/10.1021/acs.chemrev.5b00562
14. Knowles TPJ, Buehler MJ (2011) Nanomechanics of functional and pathological amyloid materials. Nat Nanotechnol 6:469–479. https://doi.org/10.1038/nnano.2011.102
15. Mei J, Leung NLC, Kwok RTK et al (2015) Aggregation-induced emission: together we shine, united we soar! Chem Rev 115:11718–11940. https://doi.org/10.1021/acs.chemrev.5b00263
16. Lim X (2016) The nanolight revolution is coming. Nature 531:26–28. https://doi.org/10.1038/531026a
17. Luo J, Xie Z, Lam JWY et al (2001) Aggregation-induced emission of 1-methyl-1, 2, 3, 4, 5-pentaphenylsilole. Chem Commun 24:1740–1741. https://doi.org/10.1039/b105159h
18. Fan Z, Sun L, Huang Y et al (2016) Bioinspired fluorescent dipeptide nanoparticles for targeted cancer cell imaging and real-time monitoring of drug release. Nat Nanotechnol 11:388–394. https://doi.org/10.1038/nnano.2015.312
19. Tao K, Fan Z, Sun L et al (2018) Quantum confined peptide assemblies with tunable visible to near-infrared spectral range. Nat Commun 9:3217. https://doi.org/10.1038/s41467-018-05568-9
20. Gao Y, Zhao F, Wang Q et al (2010) Small peptide nanofibers as the matrices of molecular hydrogels for mimicking enzymes and enhancing the activity of enzymes. Chem Soc Rev 39:3425–3433. https://doi.org/10.1039/b919450a
21. Günes S, Neugebauer H, Sariciftci NS (2007) Conjugated polymer-based organic solar cells. Chem Rev 107:1324–1338. https://doi.org/10.1021/cr050149z
22. Mishra A, Bäuerle P (2012) Small molecule organic semiconductors on the move: promises for future solar energy technology. Angew Chem Int Edit 51:2020–2067. https://doi.org/10.1002/anie.201102326
23. Hauser CAE, Zhang S (2010) Peptides as biological semiconductors. Nature 468:516–517. https://doi.org/10.1038/468516a
24. Marvin CW, Grim HM, Miller NC et al (2017) Interplay among sequence, folding propensity, and bio-piezoelectric response in short peptides and peptoids. J Phys Chem B 121:10269–10275. https://doi.org/10.1021/acs.jpcb.7b10085
25. Liu P, Pan C, Wang ZL (2018) Two-dimensional nanomaterials for novel piezotronics and piezophototronics. Mater Today Nano 4:17–31. https://doi.org/10.1016/j.mtnano.2018.11.006
26. Zelenovskii PS, Romanyuk K, Liberato MS et al (2021) 2D layered dipeptide crystals for piezoelectric applications. Adv Funct Mater 31:2102524. https://doi.org/10.1002/adfm.202102524
27. Argaman N, Makov G (2000) Density functional theory: an introduction. Am J Phys 68:69–79. https://doi.org/10.1119/1.19375
28. Hafner J (2007) Materials simulations using VASP—a quantum perspective to materials science. Comput Phys Commun 177:6–13. https://doi.org/10.1016/j.cpc.2007.02.045

29. Perdew JP, Chevary JA, Vosko SH et al (1992) Atoms, molecules, solids, and surfaces: applications of the generalized gradient approximation for exchange and correlation. Phys Rev B 46:6671–6687. https://doi.org/10.1103/physrevb.46.6671
30. Grimme S, Antony J, Ehrlich S et al (2010) A consistent and accurate ab initio parametrization of density functional dispersion correction (DFT-D) for the 94 elements H-Pu. J Chem Phys 132:154104. https://doi.org/10.1063/1.3382344
31. Kresse G, Joubert D (1999) From ultrasoft pseudopotentials to the projector augmented-wave method. Phys Rev B 59:1758–1775. https://doi.org/10.1103/PhysRevB.59.1758
32. Wu X, Vanderbilt D, Hamann D (2005) Systematic treatment of displacements, strains, and electric fields in density-functional perturbation theory. Phys Rev B 72:035105. https://doi.org/10.1103/PhysRevB.72.035105
33. Chung DH, Buessem WR (1967) The Voigt-Reuss-Hill approximation and elastic moduli of polycrystalline MgO, $CaF_2$, β-ZnS, ZnSe, and CdTe. J Appl Phys 38:2535–2540. https://doi.org/10.1063/1.1709944
34. Zuo L, Humbert M, Esling C (1992) Elastic properties of polycrystals in the Voigt-Reuss-Hill approximation. J Appl Cryst 25:751–755. https://doi.org/10.1107/S0021889892004874
35. Momma K, Izumi F (2011) VESTA 3 for three-dimensional visualization of crystal, volumetric and morphology data. J Appl Cryst 44:1272–1276. https://doi.org/10.1107/S0021889811038970
36. Tao K, Xue B, Li Q et al (2019) Stable and optoelectronic dipeptide assemblies for power harvesting. Mater Today 30:10–16. https://doi.org/10.1016/j.mattod.2019.04.002
37. Tao K, Hu W, Xue B et al (2019) Bioinspired stable and photoluminescent assemblies for power generation. Adv Mater 31:1807481. https://doi.org/10.1002/adma.201807481
38. Tao K, O'Donnell J, Yuan H et al (2020) Accelerated charge transfer in water-layered peptide assemblies. Energy Environ Sci 13:96–101. https://doi.org/10.1039/c9ee02875g
39. Bystrov VS, Coutinho J, Zhulyabina OA et al (2021) Modeling and physical properties of diphenylalanine peptide nanotubes containing water molecules. Ferroelectrics 574:78–91. https://doi.org/10.1080/00150193.2021.1888051
40. Berger O, Adler-Abramovich L, Levy-Sakin M et al (2015) Light-emitting self-assembled peptide nucleic acids exhibit both stacking interactions and Watson-Crick base pairing. Nat Nanotechnol 10:353–360. https://doi.org/10.1038/nnano.2015.27
41. Hod O (2012) Graphite and hexagonal boron-nitride have the same interlayer distance. Why? J Chem Theory Comput 8:1360–1369. https://doi.org/10.1021/ct200880m
42. Tao K, Tang Y, Rencus-Lazar S et al (2020) Bioinspired supramolecular packing enables high thermo-sustainability. Angew Chem 132:19199–19203. https://doi.org/10.1002/anie.202008702
43. Azuri I, Adler-Abramovich L, Gazit E et al (2014) Why are diphenylalanine-based peptide nanostructures so rigid? Insights from first principles calculations. J Am Chem Soc 136:963–969. https://doi.org/10.1021/ja408713x
44. Knowles TP, Fitzpatrick AW, Meehan S et al (2007) Role of intermolecular forces in defining material properties of protein nanofibrils. Science 318:1900–1903. https://doi.org/10.1126/science.1150057
45. Ranganathan S, Maji SK, Padinhateeri R (2016) Defining a physical basis for diversity in protein self-assemblies using a minimal model. J Am Chem Soc 138:13911–13922. https://doi.org/10.1021/jacs.6b06433
46. Papageorgiou DG, Kinloch IA, Young RJ (2017) Mechanical properties of graphene and graphene-based nanocomposites. Prog Mater Sci 90:75–127. https://doi.org/10.1016/j.pmatsci.2017.07.004
47. Frank IW, Tanenbaum DM, van der Zande AM et al (2007) Mechanical properties of suspended graphene sheets. J Vac Sc Technol B 25:2558–2561. https://doi.org/10.1116/1.2789446
48. Mei J, Hong Y, Lam JWY et al (2014) Aggregation-induced emission: the whole is more brilliant than the parts. Adv Mater 26:5429–5479. https://doi.org/10.1002/adma.201401356
49. Chattopadhyay A, Haldar S (2014) Dynamic insight into protein structure utilizing red edge excitation shift. Acc Chem Res 47:12–19. https://doi.org/10.1021/ar400006z
50. Rosenman G, Beker P, Koren I et al (2011) Bioinspired peptide nanotubes: deposition technology, basic physics and nanotechnology applications. J Pept Sci 17:75–87. https://doi.org/10.1002/psc.1326
51. Kasotakis E, Mossou E, Adler-Abramovich L et al (2009) Design of metal-binding sites onto self-assembled peptide fibrils. Biopolymers 92:164–172. https://doi.org/10.1002/bip.21163
52. Bank-Srour B, Becker P, Krasovitsky L et al (2013) Physical vapor deposition of peptide nanostructures. Polym J 45:494–503. https://doi.org/10.1038/pj.2013.19
53. Sun M, Luo C, Xu L et al (2005) Artificial lotus leaf by nanocasting. Langmuir 21:8978–8981. https://doi.org/10.1021/la050316q
54. Lipomi DJ, Vosgueritchian M, Tee BCK et al (2011) Skin-like pressure and strain sensors based on transparent elastic films of carbon nanotubes. Nat Nanotechnol 6:788–792. https://doi.org/10.1038/nnano.2011.184
55. Wu P, Wang J, Jiang L (2020) Bio-inspired photonic crystal patterns. Mater Horiz 7:338–365. https://doi.org/10.1039/C9MH01389J
56. Gu L, Shi H, Bian L et al (2019) Colour-tunable ultra-long organic phosphorescence of a single-component molecular crystal. Nat Photonics 13:406–411. https://doi.org/10.1038/s41566-019-0408-4